International Journal of Fatigue 70 (2015) 137–145

Contents lists available at ScienceDirect

International Journal of Fatigue

journal homepage: www.elsevier.com/locate/ijfatigue

Impact of hydrogen on the high cycle fatigue behaviour of Inconel 718 in asymmetric push–pull mode at room temperature

M. Bruchhausen [a,*], B. Fischer [a], A. Ruiz [a], S. González [a], P. Hähner [a], S. Soller [b]

[a] European Commission, Joint Research Centre (JRC), Institute for Energy and Transport (IET), Westerduinweg 3, 1755 LE Petten, Netherlands
[b] Airbus Defence And Space, Launcher Propulsion – Advanced Programs & Systems Technologies, Germany

ARTICLE INFO

Article history:
Received 4 June 2014
Received in revised form 5 September 2014
Accepted 8 September 2014
Available online 16 September 2014

Keywords:
High cycle fatigue
Hydrogen embrittlement
Inconel 718

ABSTRACT

The influence of hydrogen on the high cycle fatigue (HCF) behaviour of Inconel 718 has been studied at room temperature in asymmetric push–pull mode using an ultrasonic HCF test rig. Fatigue tests have been carried out in gaseous hydrogen (GH2) and in Ar at a pressure of 30 MPa. Oscillating stresses with amplitudes (σ_a) up to 450 MPa and mean stresses (σ_m) up to 600 MPa have been applied. For a given σ_a and σ_m, the lifetime in Ar is generally longer than in GH2, which is explained by a hydrogen-induced embrittlement of the material. For a constant σ_a of 218 MPa, the lifetime in Ar and in GH2 is very similar for high σ_m, but the difference in lifetime increases as the mean stress decreases. An approach is presented to describe the number of cycles to failure N_f as a function of σ_a and σ_m.

Microstructural analysis has been performed on the specimens tested at $\sigma_a = 218$ MPa and two values of σ_m (300 MPa and 600 MPa). SEM analyses of the fracture surfaces of these samples indicate embrittlement of the material when tested in hydrogen atmosphere.

1. Introduction

Gas phase embrittlement of materials caused by the presence of damaging species such as oxygen, hydrogen, sulphur or chlorine has been an important issue for a number of industries over the years. At least since the end of the 1950s, hydrogen is known to have a deleterious effect on the mechanical properties of many materials [1–4]. Among these materials, Ni-based superalloys, which are widely used in stationary gas turbines and liquid rocket engines because of their high strength and good corrosion resistance, are sensitive to hydrogen embrittlement [5,6]. The presence of hydrogen inside the material can originate from the material's processing or from a hydrogen-rich environment through diffusion. Due to its small size, the hydrogen atom diffuses more rapidly than larger atoms. Considering that diffusion is a thermally activated process, the temperature at which the tests are done and also the time, i.e. number of cycles, to failure are decisive. Moreover, hydrogen tends to be attracted to regions of triaxial tensile stress where the crystalline lattice is dilated and thus, it is drawn to regions ahead of cracks under stress [7,8]. For this reason, the diffusion of hydrogen is facilitated by the formation of cracks during fatigue tests.

Increasing lifetime of many engineering components has led to a growing need for materials data and in particular for fatigue data at high number of cycles. To satisfy this demand, fatigue testing by ultrasonic excitation has been pioneered in the second half of the 20th century [9] and has since been established as a means for testing to 10^9 cycles and beyond. Since the technique probes only a small volume it is also well suited for testing welds [10]. An extensive description of ultrasonic high cycle fatigue (HCF) test techniques can be found in the literature [11–13]. However, open data on the effect of hydrogen and the stress conditions on the fatigue behaviour of Inconel 718 is incomplete. In this paper the dependence of the fatigue life of Inconel 718 on the environment and stress conditions is studied with the aim of characterising the impact of a high pressure (30 MPa) gaseous hydrogen (GH2) atmosphere on the HCF behaviour of Inconcel 718 in the range of 10^6–10^7 cycles.

2. Experimental details

2.1. Material

The nominal chemical composition of Inconel 718 is shown in Table 1. Table 2 lists some basic mechanical properties. The alloy has been solution annealed and precipitation hardened (Table 3) to bring it into high strength state. The heat treatments, which

* Corresponding author.
E-mail address: matthias.bruchhausen@ec.europa.eu (M. Bruchhausen).

http://dx.doi.org/10.1016/j.ijfatigue.2014.09.005
0142-1123/

Table 1
Chemical composition of Inconel 718 (wt.%).

Al	B	C	Co	Cr	Cu	Fe	Mg	Mn	Mo
0.50	0.0033	0.009	0.53	17.88	0.03	18.28	0.0006	0.09	2.97
N	Nb	Ni	O	P	S	Si	Sn	Ti	
0.006	5.02	53.6	0.0005	<0.005	0.0008	<0.05	0.0031	0.94	

Table 2
Some basic properties of Inconel 718 at room temperature: ultimate tensile strength (σ_{UTS}), yield strength ($\sigma_{0.2\%}$), dynamic Young's modulus (E_{dyn}), and density (ρ) [14].

σ_{UTS} (MPa)	$\sigma_{0.2\%}$ (MPa)	E_{dyn} (GPa)	ρ (g/cm^3)
1395	1175	200	8.23

Table 3
Heat treatments to bring Inconel 718 in high-strength condition. All treatments were carried out in air.

Temperature (°C)	Duration	Cooling
1040	40 min	Water quench
720	8 h	Furnace cooling to 620 ° C; cooling rate −80 °C/h
620	8 h	Furnace cooling to RT; cooling rate −80 °C/h

were carried out in air, ensure that the alloying elements first are totally dissolved into the matrix before being precipitated. The resulting oxide layer formed after cooling was removed during the manufacturing of the specimens.

2.2. Test rig and specimens

The tests were carried out by means of an ultrasonic HCF test rig. Fig. 1 shows a scheme of the autoclave, the core part of the test setup. The setup has been developed for carrying out HCF tests in gaseous environments in asymmetric push–pull mode, i.e. at stress ratios $R > -1$, where R is the ratio of minimum and maximum stress σ_{min} and σ_{max}:

$$R = \frac{\sigma_{min}}{\sigma_{max}} \quad (1)$$

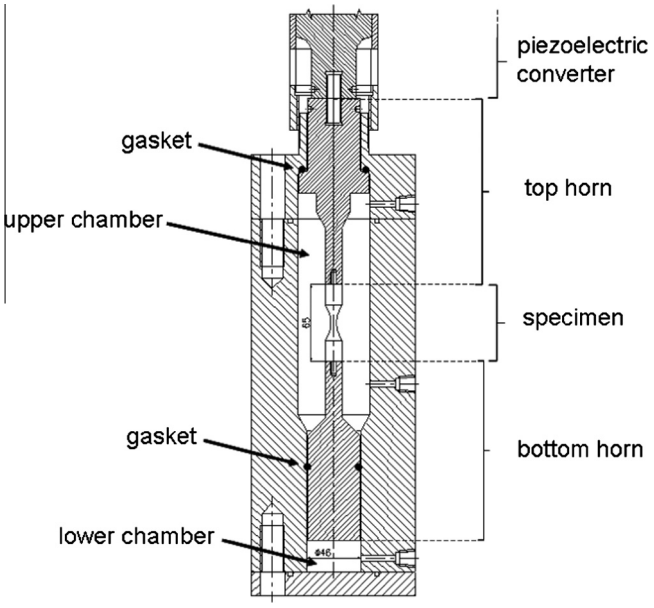

Fig. 1. Schematic layout of the experimental setup. The autoclave contains the test specimen and two acoustic horns. The lower horn divides the autoclave into two pressure chambers. The black dots at the bottom horn indicate the position of the O-ring separating the upper and lower pressure chambers.

The symmetric stress generated by ultrasonic excitation is superposed to a static stress resulting from a pressure difference. Before the test, the specimen is mounted between two acoustic horns. The upper horn is fixed to a piezoelectric transducer that converts an AC signal into mechanical oscillations at the test frequency of 20 kHz. The oscillating components are dimensioned to be in resonance with the test frequency so that a longitudinal standing wave can form. The function of the upper horn is to amplify the mechanical oscillations and to transfer them from the piezoelectric converter to the specimen. The reduction of the horn's diameter leads to an increase of the oscillating stress amplitude σ_a. The horn also serves as a lid closing the top of the autoclave.

Beneath the specimen, a second horn is mounted dividing the autoclave volume into two separate pressure chambers. The upper chamber contains the specimen in hydrogen or argon gas at a certain pressure, i.e., 30 MPa in the present test series. The lower chamber is filled with the same gas at a different (generally lower) pressure. The lower horn is fixed to the specimen and although a gasket is placed between the lower horn and the autoclave walls, the horn can move freely with regard to the autoclave wall. The lower horn is dimensioned to be in resonance with the excitation frequency of 20 kHz so it does not affect the standing wave in the load train. The gasket is positioned at a node of displacement of the lower horn to avoid damping of the oscillation as well as wear of the gasket by friction between the gasket and the autoclave wall. The pressure difference between the two chambers leads to a static force on all components of the load train, and in particular on the specimen. This force results in a static mean stress σ_m in the waist section of the specimen. A drawing of the specimen is shown in Fig. 2. The hourglass form leads to a maximisation of the mean and oscillating stresses at the specimen centre thus leading to failure at a position where the stress levels are known.

By adjusting the excitation voltage of the piezoelectric element and the pressure difference between the two chambers, the oscillating stress amplitude σ_a and the static stress σ_m can be controlled independently.

The specimens were not charged with hydrogen before testing. After installation of the specimens the test chamber was several times filled with the test gas at 1 MPa and purged. To avoid putting an undesired stress onto the specimen before the actual test, both pressure chambers were first brought synchronously to the lower of the two pressures, i.e. the pressure of the bottom chamber. Then the pressure in the upper chamber was increased to establish the environmental conditions for the test (30 MPa of GH2 or Ar). Once stable pressure conditions had been reached, the oscillating part of the stress was applied by manually starting the piezoelectric converter.

It has been shown experimentally that the specimen remains at room temperature without additional cooling. Monitoring the res-

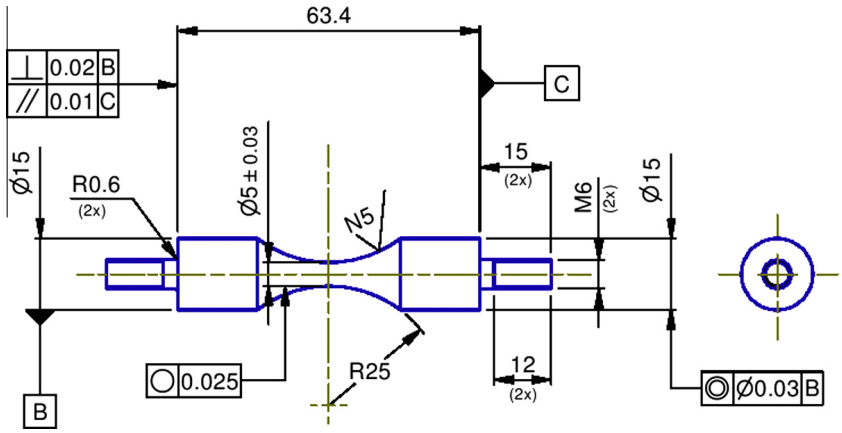

Fig. 2. Drawing of the HCF specimen.

onance frequency during the test is sufficient to verify constant temperature during the test [13].

2.3. Micro-structural characterisation

The microstructure and fracture surface of the samples were observed with a scanning electron microscope (SEM) (Zeiss Supra 50) equipped with energy dispersive X-ray (EDX) analysis. The samples of the bulk material were prepard for the SEM analysis by polishing followed by etching with glyceregia. Their structure was studied by X-ray diffraction (XRD) in a Panalytical Empyrean X-ray diffractometer using monochromated Cu K radiation and operated at a high voltage of 45 kV and anode current of 40 mA. The diffractograms were recorded from 40° to 100°, with a step size of 0.04° and time-per-step of 125 s.

3. Results and discussion

3.1. HCF lifetimes

Fig. 3 shows the lifetime of Inconel 718 in HCF tests carried out in argon and hydrogen as a function of mean stress σ_m and stress amplitude σ_a [15]. The test conditions and results are listed in Tables 6 and 7 in the appendix. In one case the test was stopped before specimen failure (dashed line). It has to be noted that three tests were carried out at somewhat higher gas pressures. These were two tests in 35 MPa Ar ($\sigma_m = 385$ MPa, $\sigma_a = 343$ MPa and $\sigma_m = 491$ MPa, $\sigma_a = 0$ MPa) and one test in GH2 at 32 MPa ($\sigma_m = 189$ MPa, $\sigma_a = 343$ MPa). These differences in pressure, however, are not believed to have significant impact on the fatigue test (see also Figs. 8 and 9).

The lifetime decreases as the mean stress or stress amplitude increase. For example, the lifetime in Ar at $\sigma_m = 500$ MPa is $7.79 \cdot 10^7$ cycles when tested at $\sigma_a = 164$ MPa but $4.10 \cdot 10^6$ cycles at $\sigma_a = 218$ MPa. Regarding environmental factors, it is observed that the lifetime of the samples tested in GH2 is in general shorter than in Ar under the same stress conditions. For example, for $\sigma_m = 300$ MPa and $\sigma_a = 218$ MPa the lifetime in Ar is $4.15 \cdot 10^7$ cycles but only $4.66 \cdot 10^6$ cycles in GH2.

In Fig. 4 the data points have been plotted in the mean stress vs. stress amplitude plane. The stress region of the investigation was chosen as to accommodate lifetimes of 10^6 to 10^7 cycles and the operation limits of the available generator (Branson PGB 220 A) at low amplitudes [13].

On the convex hull of the test area, a two-dimensional fit of N_f as a function of σ_a and σ_m has been carried out. The interrupted test in Ar was not taken into account nor were the two tests at

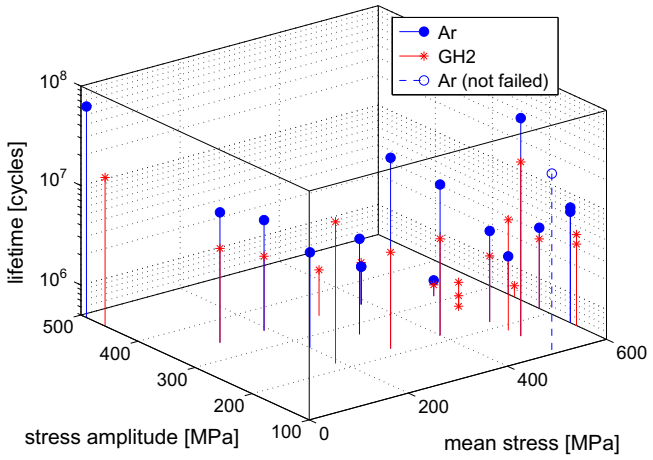

Fig. 3. HCF test results of Inconel 718 in GH2 and Ar. The dashed line stands for a test that was stopped before failure of the specimen.

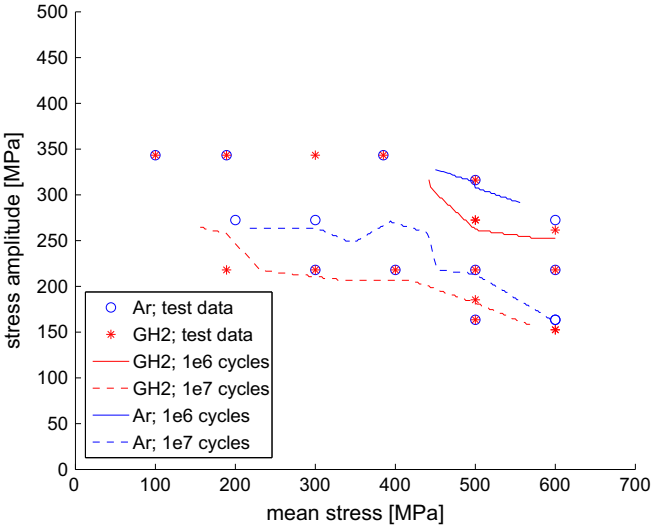

Fig. 4. Haigh diagram of Inconel 718 in GH2 and Ar with isolines for 10^6 and 10^7 cycles.

$R = -1$ ($\sigma_m = 0$). Including the tests at $R = -1$ would have resulted in an unrealistic bending of the isolines for low σ_m because of the insufficient number of data points in that area.

Based on this interpolation two isolines for $N_f = 10^6$ and $N_f = 10^7$ cycles have been obtained. The kinks in the isolines (especially for the 10^6 cycles line in Ar) are artefacts of the fitting caused by the irregular spacing of the data points. Nevertheless, it is clear from the plot that the isolines for the tests in GH2 are shifted towards lower stresses compared to the corresponding lines in Ar environment.

For a closer look on the influence of hydrogen on the mechanical performance, the mean stress has been plotted vs. lifetime for a stress amplitude of $\sigma_a = 218$ MPa (Fig. 5) and and the constant stress vs. lifetime for a mean stress of $\sigma_m = 500$ MPa (Fig. 6). The dashed lines are power law fits according to a Basquin type relationship:

$$\sigma_f = AN_f^B \tag{2}$$

where σ_f is either the mean stress or the stress amplitude at which failure occurs after N_f cycles. A and B are fitting parameters as compiled in Table 4. The coefficients of determination R^2 were calculated from the logarithmic form of Eq. (2). The deleterious impact of GH2 on the lifetime is clearly visible in both cases. Similar observations have already been reported for other Ni alloys and Ni containing steels [16,17]. Fig. 7 shows the ratio of the lifetimes N_f in GH2 and in Ar from the power law fits in Figs. 5 and 6.

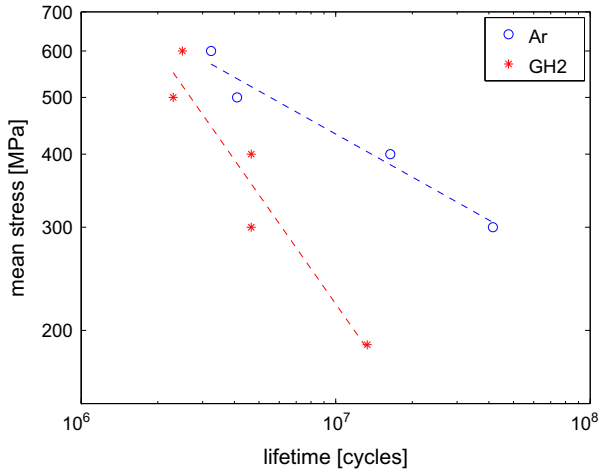

Fig. 5. Mean stress σ_m vs. cycles until failure N_f for Inconel 718 at a fixed stress amplitude $\sigma_a = 218$ MPa.

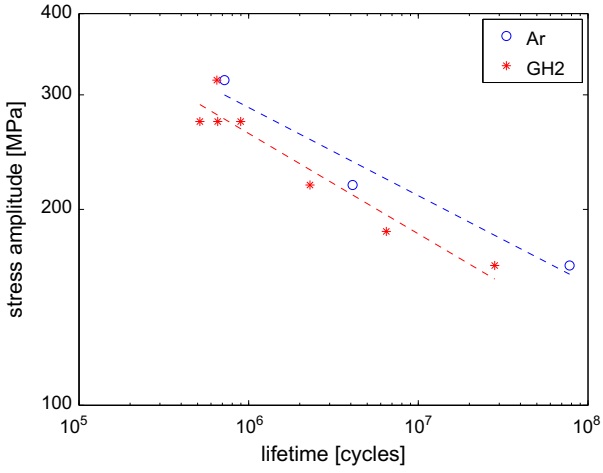

Fig. 6. Stress amplitude σ_a vs. cycles until failure N_f for Inconel 718 at a fixed mean stress $\sigma_m = 500$ MPa.

Table 4
Parameters for the power law fits in Figs. 5 and 6.

	Gas	A (MPa)	B	R^2
$\sigma_a = 218$ MPa	GH2	$4.76 \cdot 10^6$	−0.619	0.914
	Ar	$2.21 \cdot 10^4$	−0.244	0.962
$\sigma_m = 500$ MPa	GH2	$2.21 \cdot 10^3$	-0.154	0.918
	Ar	$1.86 \cdot 10^3$	−0.136	0.951

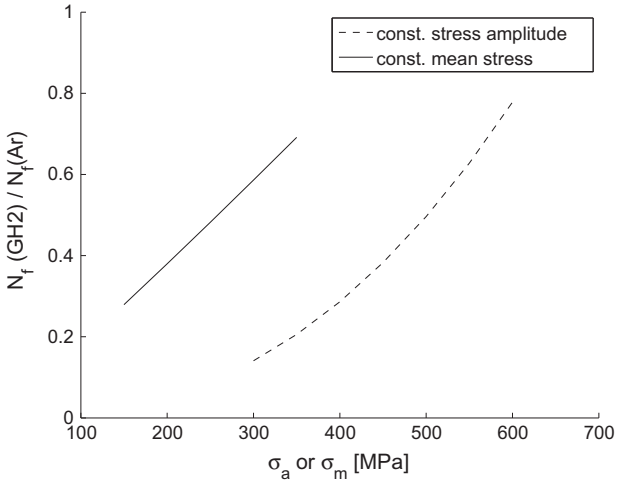

Fig. 7. Ratio of the lifetime fits N_f (Figs. 5 and 6) in GH2 and Ar as a function of mean stress σ_m at fixed stress amplitude $\sigma_a = 218$ MPa and as a function of stress amplitude σ_a at fixed mean stress $\sigma_m = 500$ MPa.

At high stress levels the lifetime in GH2 is approximately 80% of the lifetime in Ar. However, the ratio of the lifetimes in GH2 and in Ar decreases as the stress decreases and total lifetime increases. At low stress levels and correspondingly long lifetimes, the lifetime in GH2 is approxmately only 20% of the lifetime in Ar. At least for the situation studied here, the influences of the mean stress and the stress amplitude on the fatigue life are comparable. The reduced impact of hydrogen at higher alternating stress levels for Ni-base alloys has already been mentioned before [16].

That behaviour relates to the hydrogen diffusion through the sample during the test. When the samples are tested at large mean stresses failure occurs after a relatively low number of cycles. The time hydrogen has to diffuse through the sample is therefore smaller than when tested at lower stresses. On the other hand, hydrogen diffusion is accelerated by high stress levels and strong gradients which would speak for a stronger impact of hydrogen at higher stresses. The curves in Fig. 7 show that in the case studied here, the longer exposure to hydrogen is the dominant effect which is consistent with the results reported in [16].

In [17], the impact of GH2 on the fatigue behaviour of two stainless steels with different Ni content at room temperature has been studied. The tests in [17] were carried out on notched specimens at a frequency of 1 Hz. In contrast to what was observed in the present work, the authors there conclude that the negative effect of GH2 at room temperature diminishes with decreasing stress amplitudes.

Although Eq. (2) allows describing the relationship between the stresses σ_a and σ_m on one hand and the number of cycles to failure N_f on the other hand very well, it has the drawback of requiring a new set of fitting parameters A and B for every level of σ_a or σ_m. A unified description can be formulated by combining Eq. (2) with a Goodman type equation:

$$\frac{\sigma_a}{\sigma_{N_f}} + \frac{\sigma_m}{\sigma_{UTS}} = 1 \tag{3}$$

In the Goodman equation the stress amplitude σ_a is normalised by σ_{N_f}, the stress amplitude leading to failure after a certain number of cycles at fully reversed conditions (i.e. $R = -1, \sigma_m = 0$). Correspondingly, the mean stress σ_m is normalised by the failure stress at constant load conditions $(R = 1, \sigma_a = 0)$ i.e. to the ultimate tensile stress σ_{UTS}.

In order to establish a generalised formulation of Eq. (2), the Goodman equation has been modified: σ_{N_f} has been replaced by the stress amplitude σ_f at which the specimen fails after N_f cycles at a given mean stress level $\sigma_m \neq 0$ and σ_{UTS} is replaced by a parameter C'. This leads to a set of two equations with three fitting parameters A', B' and C':

$$\sigma_f = A' N_f^{B'} \tag{4}$$

$$\frac{\sigma_a}{\sigma_f} + \frac{\sigma_m}{C'} = 1 \tag{5}$$

Combining these equations allows expressing N_f as:

$$N_f = \sqrt[B']{\frac{\sigma_a}{A'\left(1 - \frac{\sigma_m}{C'}\right)}} \tag{6}$$

For fitting the parameters A', B' and C' the logarithmic form of Eq. (6) has been used where lg refers to $\log_{10}$:

$$\lg N_f = \frac{\lg\left(\frac{\sigma_a}{A'\left(1 - \frac{\sigma_m}{C'}\right)}\right)}{B'} \tag{7}$$

Figs. 8 and 9 respectively compare the experimentally observed numbers of cycles to failure $N_{f,obs}$ to the value $N_{f,pred}$ predicted by the fits in Ar and in GH2. The values for the parameters of the fits are listed in Table 5.

The fits describe the data reasonably well although the scatter is significant as confirmed by the R^2 values in Table 5. In the plots for both environments there is one outlier which is highlighted by a circle. The outliers correspond to tests performed at $R = -1$. Omitting them in the fit considerably improves the quality of the fit as characterised by the increase of $R^2 : 0.5418 \rightarrow 0.8290$ in Ar and $0.6786 \rightarrow 0.8178$ in GH2. Apparently the function defined by Eq. (6) describes the data only in a limited section of the σ_m–σ_a-plain. Since only a single test point at $R = -1$ was available for every environment these tests had little impact on the values of the fitting parameters and are not well described by the resulting function.

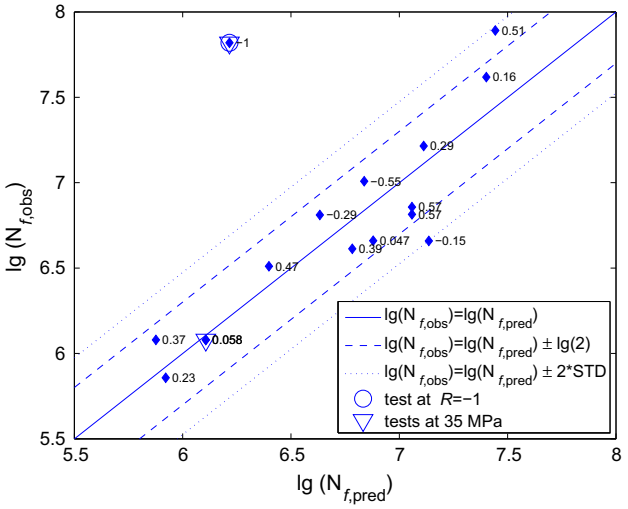

Fig. 8. Observed lifetime $N_{f,obs}$ vs. calculated lifetime $N_{f,pred}$ for Ar. The numbers next to the data points are the corresponding R-values. STD refers to the standard deviation.

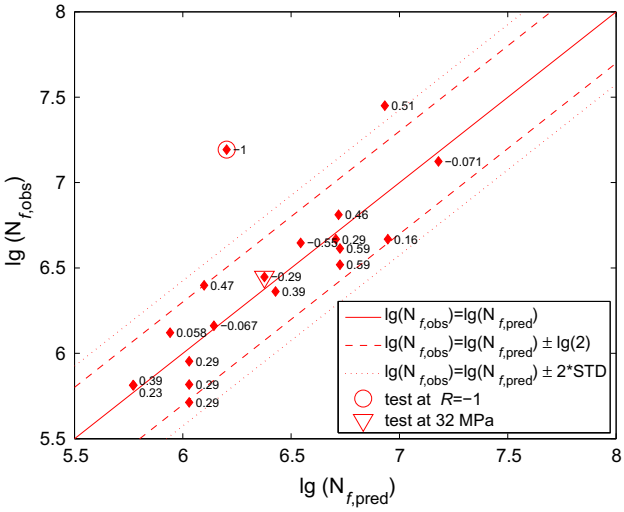

Fig. 9. Observed lifetime $N_{f,obs}$ vs. calculated lifetime $N_{f,pred}$ for GH2. The numbers next to the data points are the corresponding R-values. STD refers to the standard deviation.

Table 5
Values for the parameters in Eq. (6) in Ar and in GH2. The tests at $R = -1$ are outliers in both environments and have been discarded during the fit.

Gas	A' (MPa)	B'	C' (MPa)	R^2
Ar	7160	−0.1872	1154	0.8290
GH2	15,168	−0.2451	1089	0.8178

The observed fatigue life for $R = -1$ in Figs. 8 and 9 is much higher than predicted. A possible explanation for the particular location of these tests in the plots might come from a fracture mechanics apporoach. Fatigue life has an initiation part and propagation part. Fatigue crack propagation depends on the stress intensity [11]. In the Paris law for calculating the fatigue crack propagation rate only the stress intensity when a crack is open is accounted for, i.e. the periods of positive stresses. Thus for a given stress amplitude the effective stress intensity range is only half the value for $R = -1$ compared to $R > 0$. Alternatively one can invoke crack closure considerations to assess the influence of a compression phase on fatigue crack propagation [11]. This leads to significantly reduced crack propagation rates and a longer propagation life for $R = -1$. This effect should also be seen for all cases with $R < 0$. For $R = -0.55$ and -0.29 the observations lie slightly above the predictions but the effect is very small and these data points lie in the scatter band.

Also a purely experimental reason cannot be excluded with certainty. During the tests at $R = -1$ a bypass directly connecting the two pressure chambers was opened to guarantee the same pressure in both chambers. During the tests with $R > -1$ this bypass was closed. Opening this bypass may have led to an unexpected change of the experimental conditions. Further tests at $R \approx -1$ are needed to clarify this point.

The tests carried out at higher pressures are highlighted by triangles. But for the test in Ar at $R = -1$ they are well inline with the other data, thus confirming the insignificant influence of the variation in pressure on the fatigue life.

3.2. Microstrucural analysis

3.2.1. Bulk material

Microstructural characterisation was performed on the specimens tested at $\sigma_a = 218$ MPa and $\sigma_m = 300$ MPa and 600 MPa,

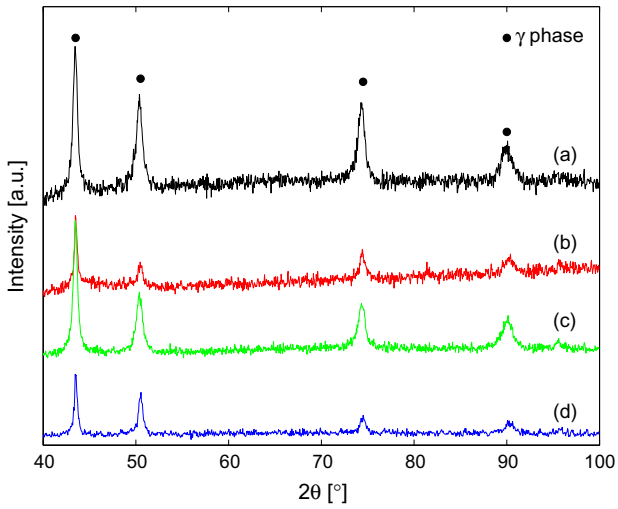

Fig. 10. XRD scans of the samples tested at $\sigma_a = 218$ MPa and $\sigma_m = 600$ MPa in (a) GH2 and (b) Ar, and at $\sigma_m = 300$ MPa in (c) GH2 and (d) Ar. To make the different spectra easily distinguishable different offsets have been added to the data.

both in Ar and GH2. Fig. 10 shows the XRD diffractograms of the four tested specimens. All analysed samples exhibit XRD peaks associated with the γ phase as described in [18]. No additional peaks at lower angles from the γ diffractions, characteristic of the β hydride phase [19], were observed. It is important to notice that the spectra were acquired after storing the samples for 3 months in air. By this time, the hydride phase has decomposed and could not be detected by XRD [19]. However, the XRD peaks after hydrogen charging at both stress conditions are slightly shifted towards smaller angles as compared to the specimens tested at the same conditions in Ar. This shift which is comparable in size to the angular resolution of the instrument suggests that some hydrogen might still be present in solid solution inside the crystalline lattice of the γ phase. This hypothesis however cannot be confirmed by EDX because of the low atomic weight of hydrogen.

Effects of the hydride decomposition could nevertheless be deduced from SEM observations in the bulk materials and in the fracture surfaces.

Fig. 11 shows SEM images of Inconel 718 tested in Ar (a,c) and in GH2 (b,d). Fig. 12 shows a magnified section of Fig. 11(d). The samples were cut from tested specimens just behind the waist, so they were exposed to almost the same stress conditions as the centre plane where failure occurred. The investigated surfaces are perpendicular to the specimen's tensile axis i.e. parallel to the fracture surfaces.

The microstructure consists of γ grains with η precipitates along the grain boundaries and the matrix as indicated by arrows in Fig. 11(c). The η precipitates formed inside each grain follow a Widmanstätten pattern with an orientation generally differing between neighbouring grains (see inset in Fig. 11(d)). These precipitates are formed during annealing to bring the alloy in high strength condition [20].

After testing in hydrogen some parallel cracks are formed inside the grains (white arrows in Fig. 12). No comparably evident cracks were found on the samples tested in Ar. Similar, albeit more obvious cracks have been observed previously in different Ni containing steels and Ni basis alloys [19]. Those cracks were caused by the decomposition of hydrides during the desorption process of

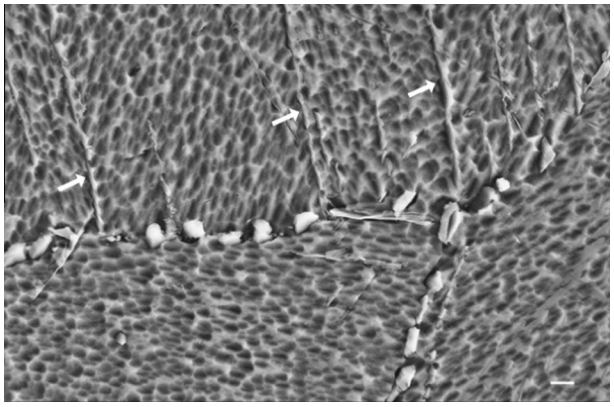

Fig. 12. Magnified image of a different area of the sample tested in hydrogen at $\sigma_a = 218$ MPa and $\sigma_m = 600$ MPa (Fig. 11(d)) presenting parallel cracks (white arrows).

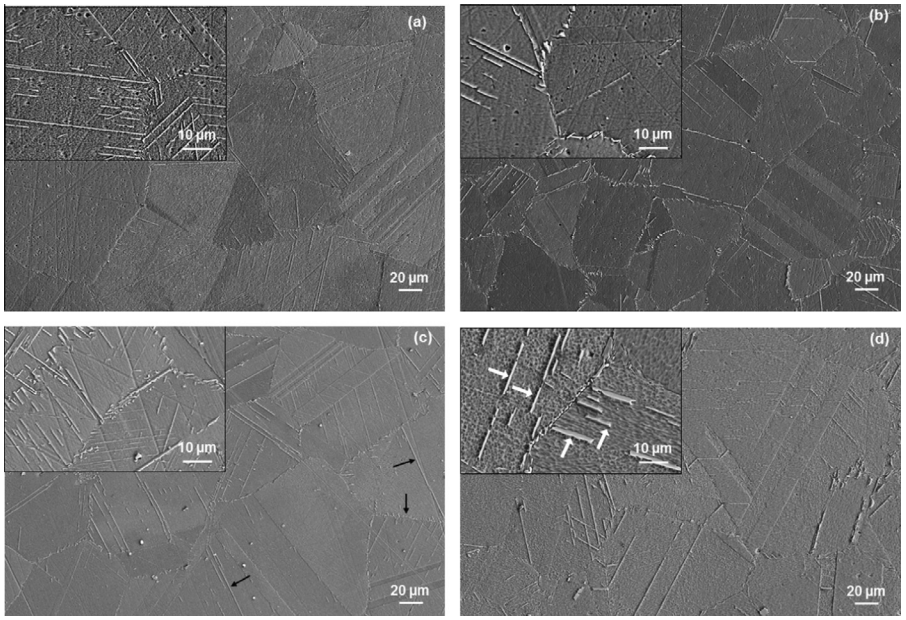

Fig. 11. SEM images of the transverse section after testing at $\sigma_a = 218$ MPa with $\sigma_m = 600$ MPa in Ar (a) and GH2 (b), and with $\sigma_m = 300$ MPa in Ar (c) and GH2 (d). The arrows point ot the η plates in the grain boundaries and the matrix.

hydrogen [19]; they were not fatigue related. It seems therefore likely that the cracks shown in Fig. 12 are also caused by hydride decomposition rather than fatigue.

3.2.2. Fracture surfaces

To better understand the influence of hydrogen on the fatigue behaviour, the fracture surfaces of selected specimens have been investigated by SEM after the fatigue tests. Figs. 13 and 14 respectively compare the fracture surfaces of specimens tested at $\sigma_m = 600$ MPa and $\sigma_m = 300$ MPa for a fixed stress amplitude of $\sigma_a = 218$ MPa. In both figures, the images on the left are from specimens tested in Ar, whereas the images on the right show specimens tested in GH2. The images in the top line (a,b) give a global view of the area of crack initiation. The insets in these images are taken at a distance from the actual initiation sites. Images (c) and (d), in the bottom row focus on the initiation sites.

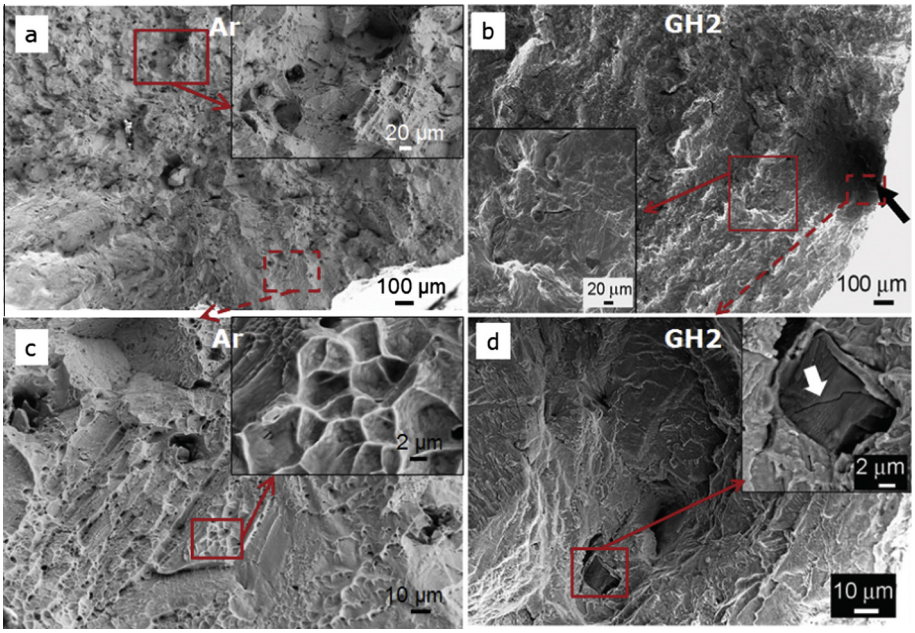

Fig. 13. SEM images of the fracture surface of Inconel 718 tested at $\sigma_m = 600$ MPa and $\sigma_a = 218$ MPa in Ar (left) and GH2 (right). (a) and (b) show the crack nucleation site and surroundings. The black arrow points at the nucleation site. Insets in (a) and (b) correspond to magnified regions further from the nucleation site. (c) and (d) focus on the nucleation sites. The white arrow in inset (d) points to the cracked particle mentioned in the text.

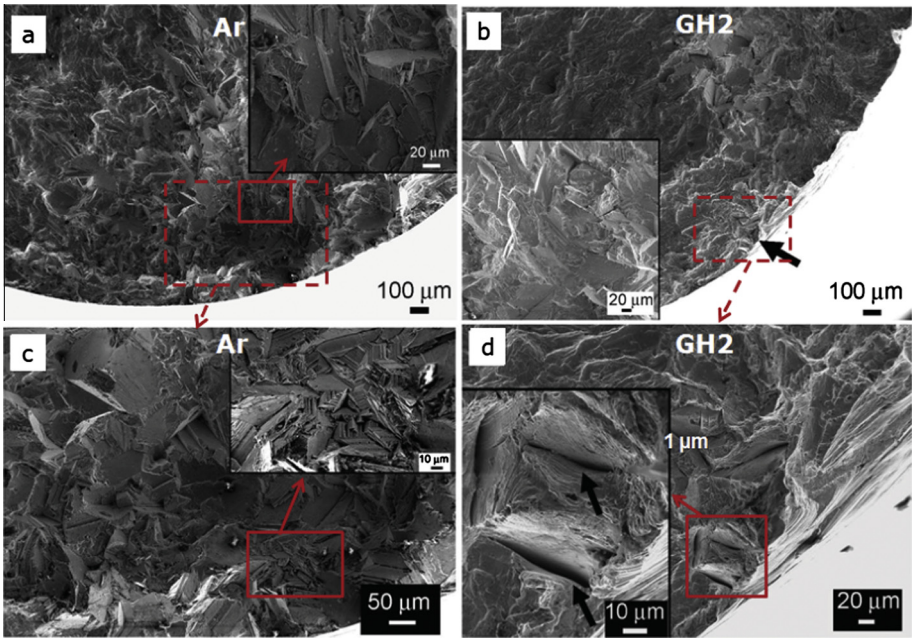

Fig. 14. SEM images of the fracture surface of Inconel 718 tested at $\sigma_m = 300$ MPa and $\sigma_a = 218$ MPa in Ar (left) and GH2 (right). (a) and (b) show the crack nucleation site and surroundings. The black arrow in (b) points at the nucleation site. The inset in (b) shows an area outside the overview image. (c) and (d) show the nucleation sites with increased magnification.

Comparing the specimens tested at the higher mean stress level ($\sigma_m = 600$ MPa) in Fig. 13 for Ar and GH2, several differences can be observed. The fracture surface of the specimen tested in Ar (a,c) clearly shows areas with a dimple structure (inset in (c)) typical for ductile fracture. In the direct vicinity of the crack nucleation site this dimpled surface morphology dominates (a) whereas further away from the nucleation site also areas with more intergranular fracture can be found (inset in (a)). This change of fracture mode with the extension of the crack for Inconel 718 has already been observed previously [21]. Such dimpled areas are not found on the specimen tested in GH2 indicating a more brittle fracture.

In the case of the test in Ar there is no well defined nucleation point whereas the crack nucleation site for the specimen tested in GH2 can be clearly identified. In GH2 a cubic particle with a size of about 10 μm was found at the nucleation site (inset in (d)). The particle was cracked due to the large stresses during fatigue testing. According to EDX analysis, this intermetallic particle is rich in Ti (43 wt.%) and Mn (10 wt.%) and could correspond to Ti_2Mn. The area in the immediate vicinity of the particle has a very ragged surface. An elongated hole of comparable dimensions above and to the right of the particle may have held another particle that has been removed from the specimen.

Looking at the fracture surfaces from the specimens tested at lower mean stress level ($\sigma_m = 300$ MPa) in Fig. 14 one can also see differences between the samples tested in Ar (a,c) and GH2 (b,d). The specimen tested in Ar shows typical facets indicative for transgranular fracture. The situation for the fracture mode of the specimen tested in GH2 is less clear; although some areas in (b) show facets, the fracture in its integrality can neither be described as clearly transgranular nor intergranular. Hydrogen seems to lead to an embrittlement of the grain boundaries resulting in a transition from essentially transgranular fracture in neutral atmosphere to a more intergranular fracture in GH2. As in the case of the higher mean stress, the specimen tested in Ar does not show a well defined crack nucleation site whereas the fracture of the specimen tested in GH2 can be traced down to a well localised spot. At the site where crack initiation occured, some deep cracks where found (highlighted by arrows in inset in Fig. 14(d)). These cracks outline a cubic geometry which suggests they may be caused by an intermetallic particle acting as stress concentrator similar to the situation found for the test at higher means stress in GH2 (Fig. 13(d)).

4. Conclusions

I. The presence of gaseous hydrogen at high pressure leads to a significant reduction of the lifetime of Inconel 718 specimens in fatigue tests.

II. The deleterious effect of hydrogen on the fatigue life of Inconel 718 specimens increases with decreasing levels of both, the mean stress and the stress amplitude.

III. A formulation using a variation of the Goodman relation for describing the number of cycles to failure N_f as a function of mean stress σ_m and stress amplitude σ_a has been found to cover most of the data well. The two tests carried out at $R = -1$, however, were not well described by this function. Further investigations are needed to clarify whether this discreapancy between the tests at $R = -1$ and the other tests can be explained by fracture mechanics or whether there is an experimental reason.

IV. The XRD scans of the specimens tested in hydrogen do not show additional peaks characteristic to hydride β phase, but the peaks associated to the γ phase are slightly shifted to smaller angles compared to the specimens tested in Ar. These results suggest that although β-hydrides decompose rapidly once the tested samples are stored, some hydrogen atoms might still remain in solid solution inside the grains.

V. SEM analyses of specimens tested at different mean stress levels have revealed signs of hydrogen embrittlement on their fracture surfaces.

Acknowledgment

Funding from the European Union Seventh Framework Programme (FP7/2007-2013) under Grant Agreement No. 218849 is gratefully acknowledged.

Appendix A

See Tables 6 and 7.

Table 6
Results for the tests in Ar.

Specimen	Pressure (MPa)	σ_a (MPa)	σ_m (MPa)	R (–)	N_f (–)	Failed (y/n)
I-01	35	343	385	0.06	1.20E+06	Y
I-02	35	491	0	−1.00	6.60E+07	Y
I-06	30	343	385	0.06	1.20E+06	Y
I-07	30	109	500	0.64	3.00E+07	N
I-08	30	316	500	0.23	7.20E+05	Y
I-09	30	218	500	0.39	4.10E+06	Y
I-10	30	164	600	0.57	7.20E+06	Y
I-11	30	273	600	0.38	1.20E+06	Y
I-19	30	164	600	0.57	6.52E+06	Y
I-20	30	343	189	−0.29	6.47E+06	Y
I-21	30	218	400	0.29	1.64E+07	Y
I-26	30	164	500	0.51	7.79E+07	Y
I-27	30	218	600	0.47	3.24E+06	Y
I-31	30	343	100	−0.55	1.02E+07	Y
I-37	30	218	300	0.16	4.15E+07	Y
I-38	30	273	300	0.05	4.57E+06	Y
I-43	30	273	200	−0.15	4.56E+06	Y

Table 7
Results for the tests in GH2

Specimen	Pressure (MPa)	σ_a (MPa)	σ_m (MPa)	R (–)	N_f (–)	Failed (y/n)
I-03	33	343	189	−0.29	2.80E+06	Y
I-12	30	458	0	−1.00	1.56E+07	Y
I-13	30	153	600	0.59	3.30E+06	Y
I-14	30	218	600	0.47	2.50E+06	Y
I-15	30	262	600	0.39	6.50E+05	Y
I-16	30	218	500	0.39	2.30E+06	Y
I-17	30	316	500	0.23	6.50E+05	Y
I-18	30	343	385	0.06	1.32E+06	Y
I-22	30	153	600	0.59	4.11E+06	Y
I-23	30	185	500	0.46	6.48E+06	Y
I-24	30	218	400	0.29	4.66E+06	Y
I-25	30	164	500	0.51	2.82E+07	Y
I-28	30	273	500	0.29	5.16E+05	Y
I-32	30	343	100	−0.55	4.43E+06	Y
I-33	30	273	500	0.29	6.57E+05	Y
I-34	30	273	500	0.29	8.98E+05	Y
I-35	30	218	189	−0.07	1.33E+07	Y
I-36	30	218	300	0.16	4.66E+06	Y
I-42	30	343	300	−0.07	1.45E+06	Y

References

[1] Cotterill P. The hydrogen embrittlement of metals. Progr Met Phys 1961;9(4):205–301.
[2] Johnson H, Troiano A. Crack initiation in hydrogenated steel. Nature 1957;179(4563):777.
[3] Williams D, Jaffee R. Relationships between impact and low-strain-rate hydrogen embrittlement of titanium alloys. J Less-Common Met 1960;2(1):42–8.
[4] Yeniscavich W, Wolfe R, Lieberman R. Hydrogen absorption by nickel enriched zircaloy-2. J Nucl Mater 1959;1(3):271–80.
[5] Jewett J, Walter R, Chandler W, Frohmberg R. Hydrogen environment embrittlement of metals. NASA contractor report NASA CR-2163; Rocketdyne; 1973.
[6] Hicks P, Alstetter C. Hydrogen-enhanced cracking of superalloys. Metall Trans A 1992;23A:237–49.
[7] Toribio J. Role of hydrostatic stress in hydrogen diffusion in pearlitic steel. J Mater Sci 1993;28:2289–98.
[8] Tsay L, Lee W, Luu W, Wu J. Effect of hydrogen environment on the notched tensile properties of *t*-250 maraging steel annealed by laser treatment. Corros Sci 2002;44:1311–27.
[9] Mason W. Internal friction and fatigue in metals at large strain amplitudes. J Acoust Soc Am 1956;28(6):1207–18.
[10] Zhu ML, Xuan FZ, Du YN, Tu ST. Very high cycle fatigue behavior of a low strength welded joint at moderate temperature. Int J Fatigue 2012;40:74–83.
[11] Mayer H. Fatigue crack growth and threshold measurements at very high frequencies. Int Mater Rev 1999;44(1):1–34.
[12] Stanzl-Tschegg S. Very high cycle fatigue measuring techniques. Int J Fatigue 2014;60:2–17.
[13] Bruchhausen M, Hähner P, Fischer B, Cornu D. Device for carrying out environmental high cycle fatigue tests with ultrasonic excitation in asymmetric push–pull mode. Int J Fatigue 2013;52:11–9.
[14] Haynes International: Haynes 718 alloy datasheet; 2011. <http://www.haynesintl.com/718HAYNESALLOY.htm>.
[15] Bruchhausen M, Fischer B. Test data for high cycle fatigue on material IN 718 at 20 °C. JRC Petten; 2013. [http://dx.doi.org/10.5290/8400004 to http://dx.doi.org/10.5290/8400036 inclusive, v1.0, data set].
[16] Balitksii A, Vytvytskii V, Ivaskevich L, Eliasz J. The high- and low-cycle fatigue behavior of Ni-contain steels and Ni-alloys in high pressure hydrogen. Int J Fatigue 2012;29:32–7.
[17] Michler T, Naumann J, Sattler E. Influence of high pressure gaseous hydrogen on sn fatigue in two austenitic stainless steels. Int J Fatigue 2013;51:1–7.
[18] Liu W, Yao M, Chen Z, Wang S. Niobium segregation in Inconel 718. J Mater Sci 1999;34:2583–6.
[19] kebir OE, Szummer A. Comparison of hydrogen embrittlement of stainless steels and nickel-base alloys. Int J Hydrogen Energy 2002;27:793–800.
[20] Zhao S, Xie X, Smith G, Patel S. Microstructural stability and mechanical properties of a new nickel-based superalloy. Mater Sci Eng, A 2003;355:96–105.
[21] Chen Q, Kawagoishi N, Wang Q, Yan N, Ono T, Hashiguchi G. Small crack behaviour and fracture of nickel-based superalloy under ultrasonic fatigue. Int J Fatigue 2005;27:1127–232.